Bioresource Technology 368 (2023) 128353

Contents lists available at ScienceDirect

Bioresource Technology

journal homepage: www.elsevier.com/locate/biortech

Pyrolysis self-activation: An environmentally friendly method to transform biowaste into activated carbon for arsenic removal

Qi Gao[a,b], Zixing Feng[a,b,1], Yuyu He[a,b], Yanmei Hou[a,b], Hao Ren[a,b], Mengfu Su[a,b], Liangmeng Ni[a,b], Zhijia Liu[a,b,*]

[a] *International Centre for Bamboo and Rattan, Beijing 100102, China*
[b] *Key Laboratory of NFGA/Beijing for Bamboo & Rattan Science and Technology, Beijing 100102, China*

HIGHLIGHTS

- Activated carbon are prepared without any added activators and auxiliary gases.
- The activated carbon exhibits excellent arsenic adsorption property.
- The mechanism of self-activation is explored and direct evidence is provided.
- The gaseous product of self-activation has a high higher heating value.

GRAPHICAL ABSTRACT

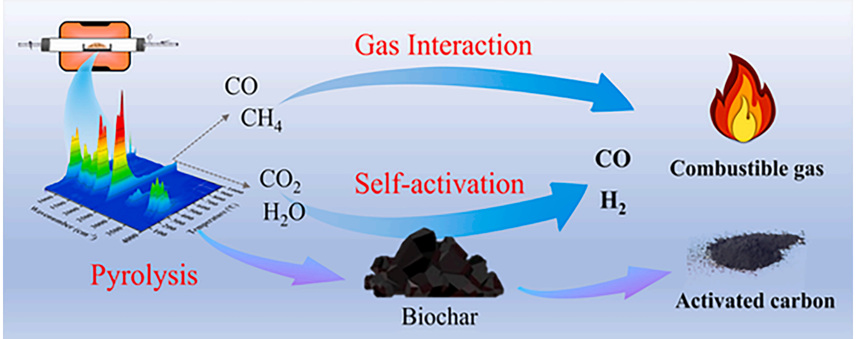

ARTICLE INFO

Keywords:
Pyrolysis
Self-activation
Activated carbon
Combustible gas
Arsenic adsorption

ABSTRACT

A green method for production of activated carbon and combustible gas was introduced. Without any external reagents and gases, the H_2O and CO_2 produced by the pyrolysis of bamboo shoot shells were used as activators. The prepared activated carbon had good arsenic adsorption properties with the maximum adsorption capacities of 10.9 mg/g for As(III) and 16.0 mg/g for As(V). The gaseous products were mostly CO and H_2, with higher heating value of 11.7 MJ/Nm^3. Thermogravimetric experiments were performed in N_2, H_2O and CO_2 atmospheres to simulate the self-activation process and investigate the self-activation mechanism. This work will help to improve the competitiveness of self-activation technology and reduce the production cost of activated carbon.

1. Introduction

Arsenic (As) is a major environmental pollutant that has received increased attention due to its toxicity and widespread distribution (Yin et al., 2019). Arsenic is found in water primarily in the forms of arsenite (As(III)) and arsenate (As(V)). (Zoroufchi Benis et al., 2021). Generally, As (V) predominates in the oxygen-rich state, while As(III) accounts for a large proportion in the anoxic environment (Zhong et al., 2021). The

---

[*] Corresponding author.
E-mail address: Liuzj@icbr.ac.cn (Z. Liu).

[1] Co-First Authors: Zixing Feng, equal contributor as first author.

https://doi.org/10.1016/j.biortech.2022.128353
Received 13 September 2022; Received in revised form 12 November 2022; Accepted 15 November 2022

conventional technologies for removing arsenic from water are adsorption, biological methods, ion exchange, coagulation, co-precipitation and membrane separation (Pincus et al., 2021). Among them, adsorption is recognized as the most effective approach due to its ease of use, high efficiency, and environmental friendliness. Activated carbon is commonly used as arsenic adsorbent due to its dense pore structure, large specific surface area, and abundance of surface functional groups. However, the high cost of activated carbon prevents widespread industrial application. As a result, it is critical to develop a low-cost method of producing activated carbon.

Biowaste is an abundant, sustainable, and low-cost feedstock to produce activated carbon (Omorogie et al., 2021). Although most biowastes can be converted into activated carbons, in most cases, an external activation agent is usually required to improve their properties, such as $ZnCl_2$, KOH, NaOH, H_3PO_4, etc. (Kleszyk et al., 2015). They not only prolong the laborious steps of washing and recovery after pyrolysis, but they also pollute the environment and cause equipment corrosion (Gayathiri et al., 2022). Physical activation needs continuous introduction of environmentally friendly agents, such as CO_2 or H_2O gas. It requires a high temperature and a long time, resulting in high energy consumption and production costs (Vinayagam et al., 2020). Therefore, it is critical to seek an energy-saving and environmentally friendly strategy for producing low-cost activated carbons.

Pyrolysis self-activation is a new green manufacturing technology for activated carbon from biomass, which reaction is carried out in a closed reactor with biomass as feedstock, and the gaseous products (CO_2 and H_2O) of biomass pyrolysis are used as activation agents (Chen et al., 2012). It avoids the cost of activator and reduces the production steps and subsequent washing process. Based on former study, activated carbon prepared by pyrolysis self-activation of cellulose at 1100 °C for 2 h presented a high specific surface area (up to 2600 m^2/g) (Bommier et al., 2015). Although no additional activator is added in this method, the flowing argon is employed during manufacturing process. Currently, a new idea of self-activation has been proposed to further reduce production costs. The pyrolysis and self-activation process of biomass are performed in a completely closed and vacuum system without introducing any additional gas or activator (Xia and Shi, 2016). Activated carbon of pine wood with a specific surface area of 692–2738 m^2/g was prepared at a temperature of 1050 °C for 2–32 h by this vacuum self-activation (Xia et al., 2016). So far, all reports on self-activation have focused solely on the properties of activated carbon, ignoring value-added utilization of gaseous products (Sulaiman et al., 2018). During the process of self-activation, CO_2 can react with C to form CO, and H_2O reacts with C to form H_2, resulting in a high concentration of combustible components in the gaseous product. It can be recycled as combustible gas because of the closed reaction environment during self-activation process. This will decrease the production cost of activated carbon and further improve commercial competitiveness of self-activation technology. To the best of our knowledge, there is still a lack of sufficient information about self-activation behavior and activation mechanism during self-activation process, limiting the development and utilization of this technology. Based on the aforementioned motivations and findings, a systematic investigation of the self-activation process is required.

Bamboo shoot shells (BSS) were used as feedstocks in this research, which are the main wastes during bamboo shoot processing. The annual yield of BSS has surpassed 30 million tons in China (Ye et al., 2014). Activated carbon was prepared by pyrolysis self-activation, and its characteristics and arsenic adsorption properties were investigated. The pyrolysis behaviors of BSS under N_2, H_2O and CO_2 atmospheres were performed to understand pore development of activated carbon and self-activation mechanism. Especially, the energy potential of gaseous products was further evaluated.

2. Materials and methods

2.1. Materials

Moso *(Phyllostachys edulis)* BSS were sampled from Zhejiang Province, China. The samples were washed (deionized water) and then pulverized after drying, and the particle sizes ranging from 180 to 250 μm were collected and dried in the oven at a temperature of 103 ± 2 °C for 12 h.

$AsNaO_2$ and $HAsNa_2O_4 \cdot 7H_2O$ (analytical grade) were purchased from Sigma-Aldrich. They were dissolved in ultrapure water to prepare As(III) and As(V) stock solutions with the concentration of 1000 mg/L. The working solutions were further obtained by diluting the above-mentioned stock solutions using ultrapure water. The pH value of solution was adjusted by NaOH and HCl.

2.2. Pyrolysis self-activation process

Pyrolysis self-activation of BSS was carried out in a custom-made tube furnace system (MGF-3, MAKEWAVE, China), which includes a tube furnace as the heating source, a thermocouple transmitter for temperature recording throughout the experiment, and a quartz tube with the length of 910 mm and diameter of 50 mm as the reactor (Fig. 1). The flanged joints are installed at both ends of the tube to facilitate the connection of vacuum pump and gas collection device. Besides, the high-purity nitrogen is added upstream of the reactor to facilitate the collection of self-activated products at specific temperatures.

The following procedures were used to produce activated carbons through pyrolysis self-activation. The crucible containing about 10 g BSS was placed into the quartz tube. A vacuum pump sucked out the air inside the reactor until the pressure reached −0.1 MPa. The valve of furnace was turned off to create a closed system. The reactor was heated to the target temperatures of 800 °C, 900 °C, 1000 °C, 1100 °C and 1200 °C for 2 h, 4 h, 6 h and 8 h at a heating rate of 5 °C/min, then it was naturally cooled to room temperature. A gas sampling bag was used to collect the gaseous products, and activated carbons (ACs) were removed from the furnace. ACs were washed using deionized water and dried in the oven at a temperature of 103 ± 2 °C for 12 h, which labelled as AC-*T*-*t* (T and t refer to temperature and time). The mass yield of ACs was calculated by equation (1):

$$\text{Yield} = (M_{BSS}/\ M_{AC}) \times 100\% \qquad (1)$$

Pore development behaviors of BSS were monitored during pyrolysis self-activation process. The samples were collected at different temperature intervals. When samples were heated to the target temperature, the furnace was purged under a high flow rate of N_2 instead of heat preservation. This was to completely remove the activation gas generated by BSS pyrolysis, and avoid the self-activation reactions during the cooling process. Therefore, the obtained samples can be regarded as the state of BSS at a given temperature during pyrolysis self-activation process.

2.3. Pyrolysis characteristics

The pyrolysis properties and gaseous products of BSS were determined through a thermogravimetric analyzer coupled with Fourier transform infrared spectrometer (TG-FTIR). The thermogravimetric (TG) experiments were conducted using SETSYS evolutive (TGA4000, PerkinElmer, USA) with a sample mass of 10 mg and N_2 flow rate of 50 ml/min. The pyrolysis temperature was controlled from room temperature to 1000 °C at a heating of 5 °C/min. The FTIR tests were performed using a spectrometer (Frontier, PerkinElmer, USA) coupled with TG for the online detection of gas-phase products and functional groups. The pyrolysis volatiles were quickly swept into an FTIR gas cell by N_2 flow. The conveying tube and FTIR gas cell were maintained at a temperature of 280 °C to avoid secondary reactions. The spectrum scope was set in

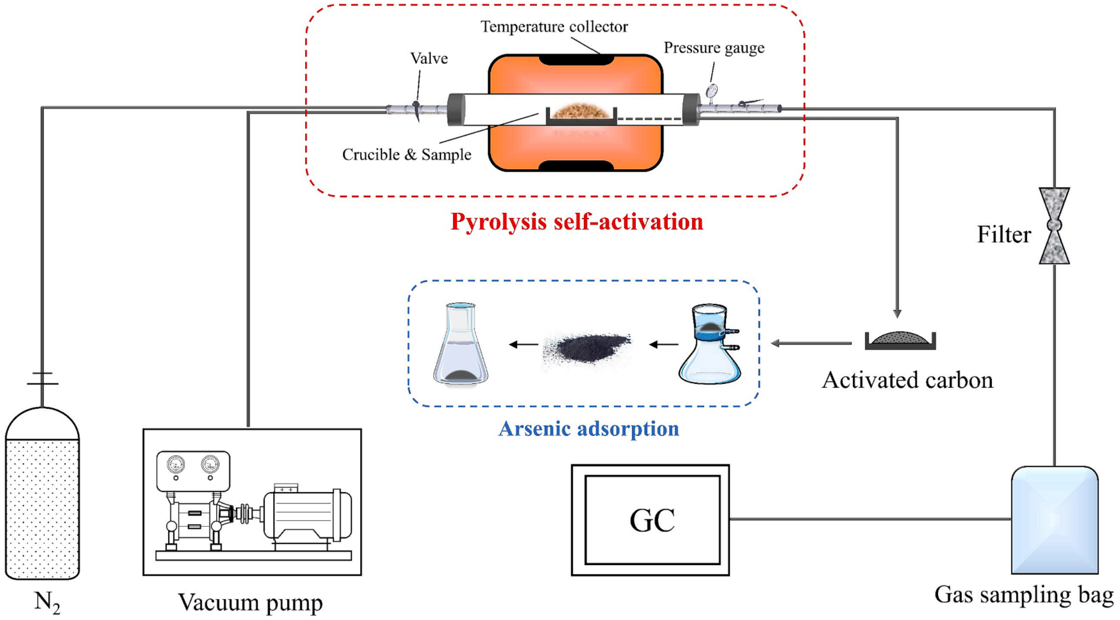

Fig. 1. Schematic diagram of pyrolysis self-activation system.

the range of 4000–500 cm^{-1} with a resolution factor of 4 cm^{-1}.

The pyrolysis characteristics of BSS in CO_2 and H_2O steam atmosphere were investigated using thermogravimetric analyzer (CO_2: TGA7300, HITACHI, Japan; H_2O steam: STA449F3, NETZSCH, Germany) to understand the self-activation mechanism. Thermogravimetric experiments were conducted with 10 mg BSS with a flow rate of 50 ml/min. The experiments were heated to 1000 °C at a heating rate of 5 °C/min. For pyrolysis of BSS under H_2O steam atmosphere, they were heated to 150 °C in N_2 and then switched to H_2O steam atmosphere. Besides, the Coats-Redfern (CR) method was used to calculate kinetic parameters of char reaction stage (Gao et al., 2022).

2.4. Characterization of products

The ACs were characterized by an N_2 adsorption/desorption tester (Autosorb IQ2, Quanta chrome, USA) (Hou et al., 2020). The morphology and structures of ACs were determined by Scanning electron microscopy (XL30, PHILIPS, Netherlands), X-ray photoelectron spectroscopy (250Xi, Thermo Scientific, USA), and Raman spectroscopic spectrometer (Lab RAM HR Evolution, HORIBA, Japan). The C, H, and N of ACs was determined by an ultimate analyzer (ADCHN335, Sundy, China) and the O element was calculated by difference. The pH zero-point charge (pH_{zpc}) of ACs were determined by salt addition method (Slimani et al., 2014).

The gaseous products were analyzed using a gas chromatograph (GC-2010, SHIMADZU, Japan). In this study, four gases were considered (H_2, CO, CH_4 and CO_2), and the total amount of these gases were specified as 100 % for comparison. Two replicates of this experiment were performed and the average value was used as the final result. The concentration of these gases was calculated by equation (2):

$$C_i = X_i/(X_{H2} + Xco + Xco_2 + Xo_2) \times 100\% \tag{2}$$

where, C_i is the relative volume fraction of *gas-i* (%), and X is the volume fraction in the sampled gas (%).

The higher heating value (HHV) of gas product was calculated by equation (3) (Chen et al., 2013):

$$HHV\left(MJ/Nm^3\right) = 11.70 \times C_{H2} + 11.55 \times C_{CO} + 36.26 \times C_{CH4} \tag{3}$$

2.5. Determination of arsenic adsorption capacity

The arsenic adsorption capacities of ACs were determined at an initial arsenic concentration of 10 mg/L and solution pH of 7. Batch adsorption experiments were carried out at temperature of 25 °C by adding 50 mg ACs to a glass container with 50 ml of arsenic solution. After shaking for 4 h at a speed of 150 rpm per minute in a rotary shaker, the supernatant was filtered by 0.45 μm PTFE syringe filter. The arsenic concentrations were determined by an inductively coupled plasma optical emission spectrometer (Optima 8X00, PERKINELMER, USA), with a limit of detections of 0.01 mg/L. Three replicates of each experiment were performed. The adsorption capacity of arsenic was calculated by equation (4):

$$q_e = V(C_0 - C_e)/m \tag{4}$$

where, q_e is the equilibrium adsorption capacity (mg/g); C_0 and C_e are the initial and equilibrium concentration of arsenic ion in solution (mg/L); V is the volume of arsenic solution (mL); m is the mass of adsorbent used in the experiment (mg).

The effects of temperatures (10–40 °C) and solution pH (2–12) on arsenic adsorption were also investigated, which kept other conditions constant. The adsorption isotherm of arsenic was recorded at different concentrations (1–100 mg/L) with the temperature of 25 °C and solution pH of 7. And the samples were taken at different time intervals for determination of the adsorption kinetics (Li et al., 2021).

3. Results and discussion

3.1. Pyrolysis characteristics

Fig. 2a depicted mass loss (TG) and mass loss rate (DTG) curves of BSS. There were three stages of mass loss during pyrolysis process, corresponding to the drying stage with temperature of 30–130 °C, the main pyrolysis stage with temperature of 130–560 °C and the secondary decomposition stage of solid residues with temperature of 560–1000 °C. When the pyrolysis temperature was raised to 560 °C, approximately 77 % of the BSS was released. The final yield of biochar was 21.7 %. The DTG curves revealed three peaks, corresponding to water evaporation at around 70 °C and organics volatilization at around 280 °C and 325 °C. To better understand pyrolysis process of BSS, the DTG curve was

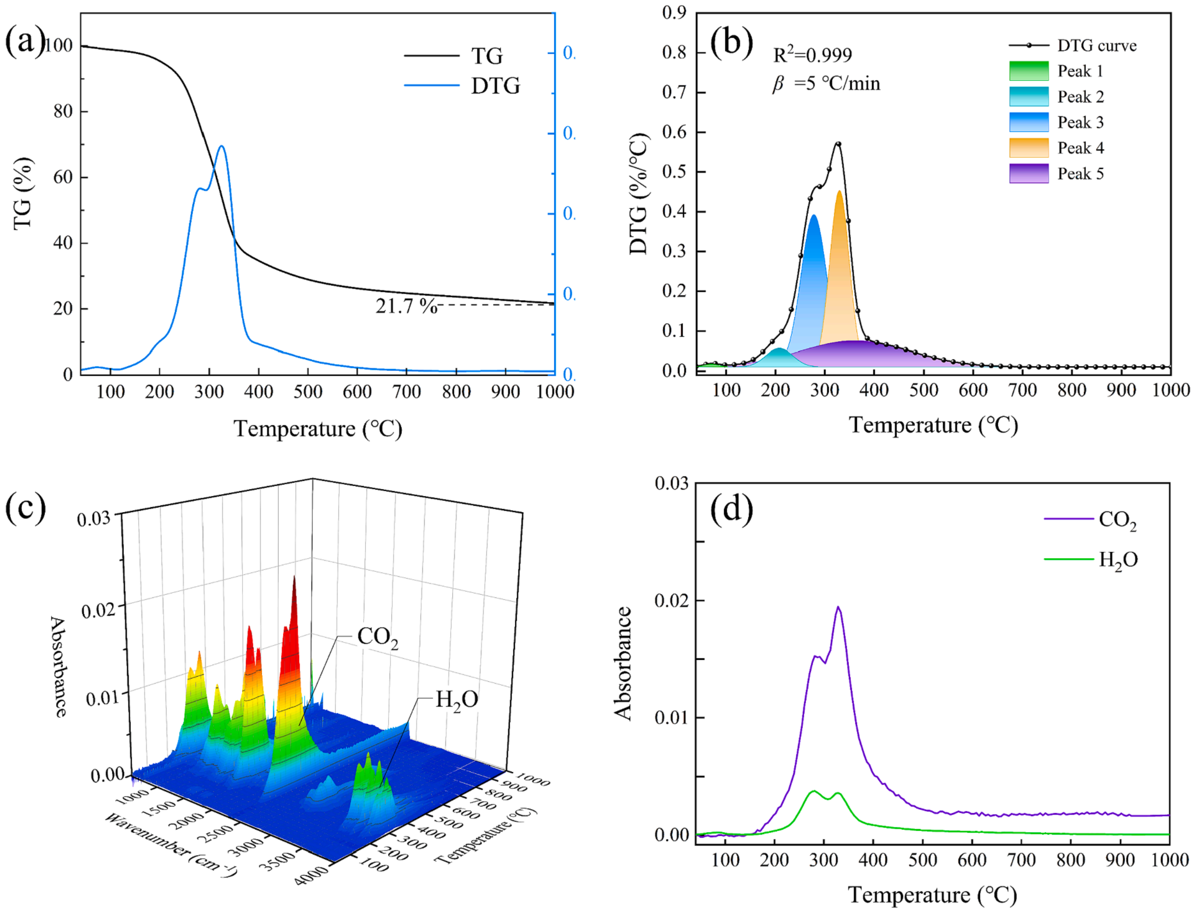

Fig. 2. Pyrolysis characteristics of BSS. (a) TG and DTG curves; (b) Split-peak fitting of DTG curve; (c) 3D infrared spectrum of pyrolysis products; (d) FTIR spectrum of CO_2 and H_2O with temperature.

divided into several simulated and individual pyrolysis peaks by Gaussian-fit-peak model (Li et al., 2017). The whole DTG curve was divided into five individual peaks, corresponding to the evaluation of water, branched and main chains of hemicellulose, cellulose, and lignin (Fig. 2b). Their peak temperatures (peak 1–5) were 70 °C, 207 °C, 278 °C, 330 °C and 361 °C, respectively. This indicated that hemicellulose, cellulose and lignin had different reactivity during pyrolysis process of BSS.

Fig. 2c showed the 3D FTIR spectrum analysis of gaseous products evolved from BSS pyrolysis. The main FTIR adsorption peaks were around 3560 cm^{-1}, 2930 cm^{-1}, 2360 cm^{-1}, 2180 cm^{-1}, 1060 cm^{-1} and 1758 cm^{-1}, corresponding to the emission of H_2O, alkanes, CO_2, CO, compounds with C═O bond, and O-including compounds (see Supplementary materials) (Chen et al., 2019). Furthermore, the H_2O and CO_2 from BSS pyrolysis were continuously recorded on a FTIR spectrophotometer as a function of pyrolysis temperature (Fig. 2d). The main emission temperatures range was 180–380 °C for the emission profile of H_2O, and there were three main absorption zones at temperatures of 80 °C, 280 °C and 330 °C. It was primarily due to the evaporation of water in BSS and dehydration reactions (R1) of hydroxyl compounds (Table 1). The weak absorption signal of –OH band at higher temperature zone (>400 °C) indicated that lignin slightly contributed to the release of H_2O. The CO_2 release had two peaks (280 °C and 330 °C), which was similar to DTG curves. Cellulose and hemicellulose were the major components of BSS, which contained a large amount of carboxyl (C═O) and COOH. Their cracking and reforming reactions (R2 and *R*3) released most CO_2 (Dong et al., 2019). When pyrolysis temperature was higher than 500 °C, there were still apparent absorption peaks of CO_2. This indicated that much O element escaped in the form of CO_2 from biochar, due to the deeply aromatization and heteroatoms removal of biochar (Wu et al., 2018). The release of H_2O and CO_2 from BSS pyrolysis could be used as activation agent of self-activation reaction.

Table 1
Main reactions during the self-activation process.

Reaction type	Reaction	Number
Pyrolysis reaction	R-OH → R· + H_2O	R (1)
	R-COOH → R-H + CO_2	R (2)
	R-C═O → R· + CO_2	R (3)
	R—C—O—C → R· + CO	R (4)
	R-C═O → R· + CO	R (5)
	R-O-CH_3 → R· + CH_4	R (6)
Activation reaction	C (s) + H_2O (g) ↔ H_2 (g) + CO (g), ΔH = 131 kJ/mol	R (7)
	C (s) + CO_2 (g) ↔ 2CO (g), ΔH = 172 kJ/mol	R (8)
	C (s) + $2H_2$ (g) ↔ CH_4 (g), ΔH = -75 kJ/mol	R (9)
Gas interaction	CH_4 (g) + H_2O (g) ↔ CO (g) + $3H_2$ (g), ΔH = 206 kJ/mol	R (10)
	CH_4 (g) + CO_2 (g) ↔ 2CO (g) + $2H_2$ (g), ΔH = 247 kJ/mol	R (11)
	CO (g) + H_2O (g) ↔ CO_2 (g) + H_2 (g), ΔH = -41 kJ/mol	R (12)

ΔH: The enthalpy of reaction, which is the theoretical value rather than the actual measured value.

3.2. *Self-activation behaviors*

In order to understand the self-activation mechanism, pyrolysis self-activation process of BSS was investigated further. The pore development behavior and mass loss of BSS during self-activation were shown in Fig. 3a. The yield curves of self-activation process had a similar trend to that of pyrolysis at the first stage with temperature of 100–700 °C. The mass and the mass loss rate of BSS gradually decreased with the increase of temperatures due to the release of volatile matters. This indicated that the first stage of pyrolysis self-activation showed conventional pyrolysis behavior. The pressure and residual air led to the variation in yields (Basile et al., 2014). Compared with pyrolysis process, the mass of BSS significantly decreased during self-activation process when temperature further increased from 700 °C to 1000 °C. This implied that BSS occurred to self-activation reaction to take away the carbon atoms, resulting in mass loss of samples. The data of pore structure further supported this conclusion. The BET surface area of BSS biochar was kept at a low level (5–11 m^2/g) until temperature of 700 °C during self-activation process. However, it significantly increased after temperature of 700 °C. The N_2 adsorption capacity and total pore volume (see Supplementary materials) showed a similar rule. The average pore size of raw BSS was 10.5 nm, which gradually decreased to 2.0 nm (1000 °C) with the increase of temperature (see Supplementary materials). This showed that a large number of pores were generated in the process of self-activation. The N_2 adsorption dates confirmed that pore structure gradually formed in BSS after temperature of 700 °C during self-activation process. Fig. 3b showed the changes of element composition of BSS during self-activation process. As the temperature rose, the elements of O, H and N escaped with the volatiles, resulting in the carbon content of BSS increasing from 50 % to 91 %.

Thermogravimetric experiments under H_2O and CO_2 atmospheres were used to simulate the activation behavior of BSS during self-activation process. Compared with the pyrolysis of BSS under N_2 atmosphere, there was an obvious mass loss at high temperature zone under H_2O or CO_2 atmosphere (Fig. 3c-d). Due to the reaction (R7) of $C + H_2O \rightarrow H_2 + CO$, the pyrolysis of BSS under H_2O atmosphere caused mass loss in the temperature range of 610–800 °C. The maximum mass loss rate was found at temperature of 770 °C. The DTG curve of pyrolysis under CO_2 atmosphere showed a sharp peak at temperature of 861 °C, and the temperature range of mass loss was 690–880 °C, corresponding to the activation reaction of R8: $C + CO_2 \rightarrow 2CO$ (Table 1). The temperature range of mass loss coincided with the activation stage during self-activation process, confirming the activation of H_2O or CO_2. The pyrolysis of biomass and activation of H_2O released some H_2, another possible activation reaction (R9) was therefore proposed: $C + 2H_2 \rightarrow CH_4$ (Bommier et al., 2015). However, the reaction of C with H_2 was exothermic, and the higher temperature shifted the equilibria of the endothermic reactions toward the products while those of the exothermic transformed to the reactants. Therefore, the high temperature environment of self-activation process was not conducive to this reaction, and the activation of H_2 was insignificant compared with H_2O or CO_2.

The active pyrolysis zones were considered for the calculation of kinetic parameters, and the Coats-Redfern method was used to determine activation energy and pre-exponential coefficient. The pre-exponential value of pyrolysis under CO_2 atmosphere (1.3×10^{11} min^{-1}) was found higher than that of pyrolysis under H_2O atmosphere (8.7×10^{7} min^{-1}). Activation energy represents the minimum energy requirement for a reaction. The higher value of activation energy means the slower reaction rate and the more difficulty to occur a reaction (Özsin and Pütün, 2017). The activation energy of BSS pyrolysis under CO_2 atmosphere (258 kJ/mol) was higher than that of H_2O atmosphere (177 kJ/mol), indicating that the activation of CO_2 during self-activation process was more difficult. The TG results showed that H_2O participated in the activation reaction earlier and required less energy during self-activation process.

3.3. Characterizations of ACs

The ACs were prepared by pyrolysis self-activation, and the effects of temperatures and residence times on its pore structure were investigated. The saturated N_2 adsorption capacity of ACs increased from 133 cm^3/g (AC-800–4) to 789 cm^3/g (AC-1200–4) with increase in activation temperatures (Fig. 4a). The N_2 adsorption isotherms of all samples

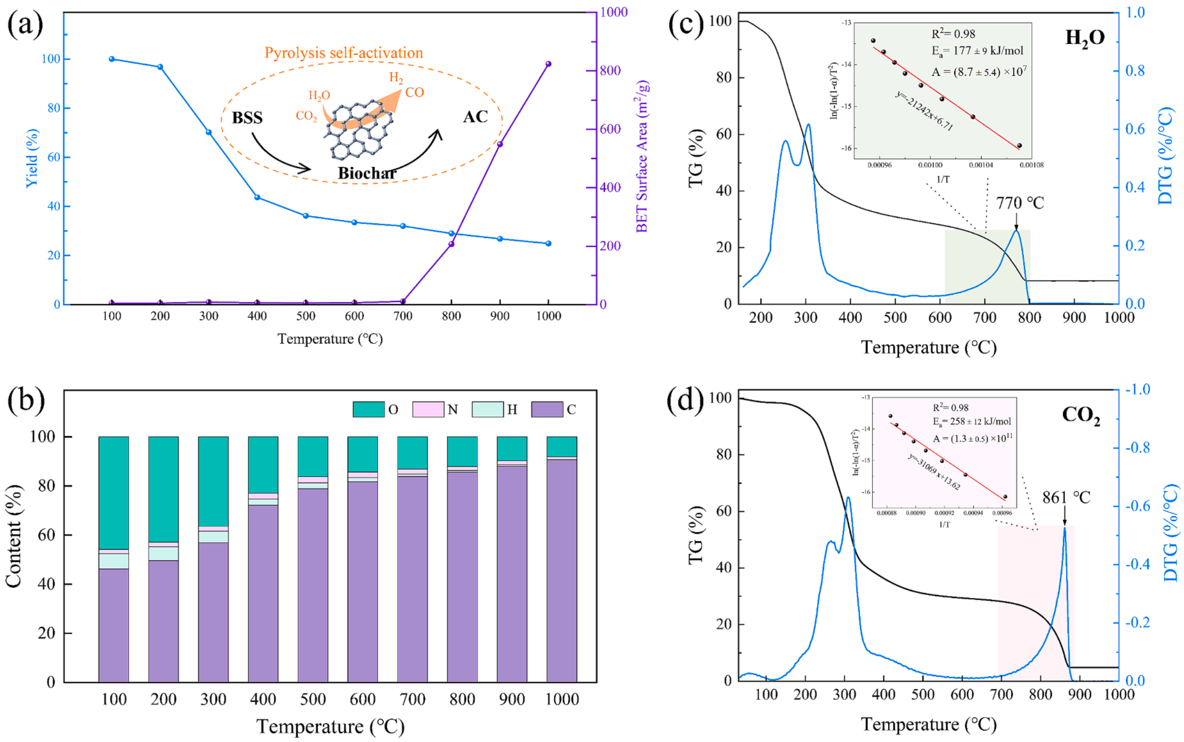

Fig. 3. Self-activation behavior of BSS. (a) Pore development and mass variation; (b) Element composition; (c) Pyrolysis under H_2O atmosphere; (d) Pyrolysis under CO_2 atmosphere.

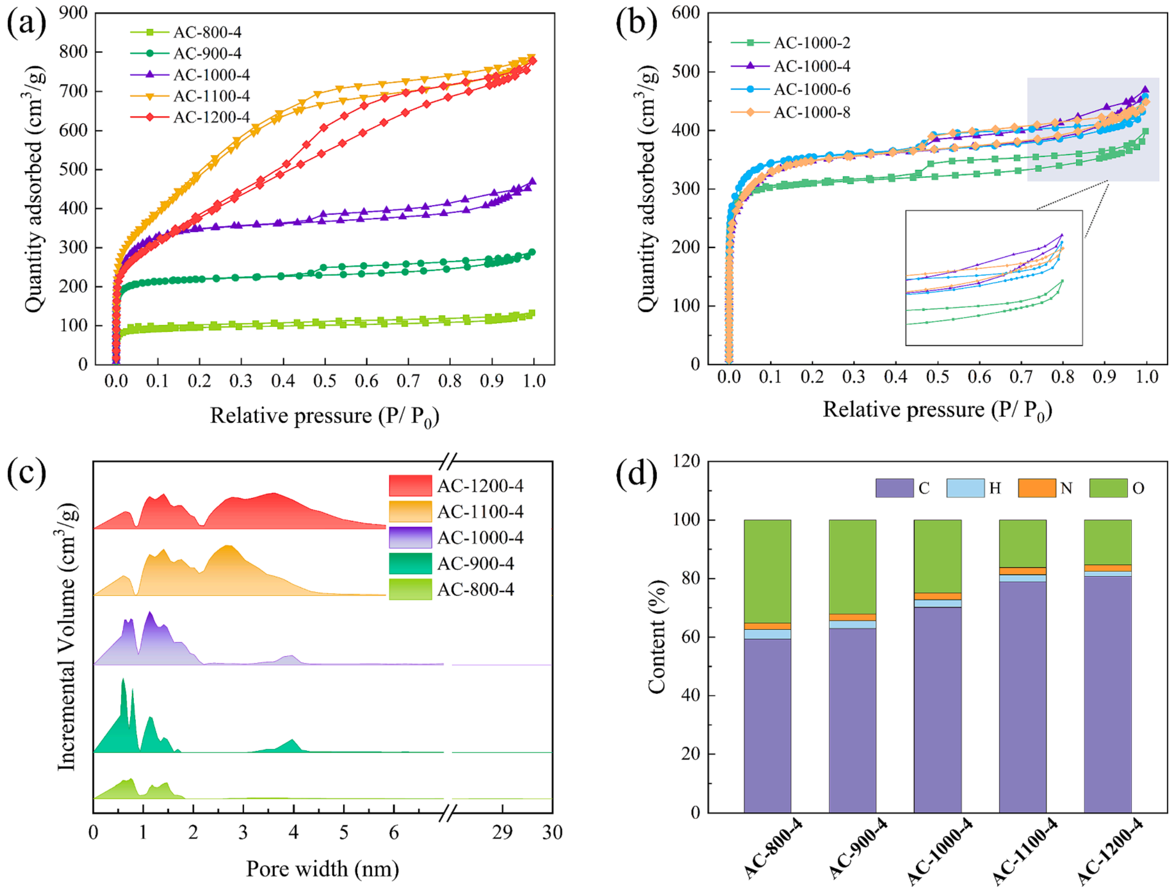

Fig. 4. Pore structure and properties of ACs. (a-b) N_2 adsorption/ desorption isotherms; (c) Pore-size distribution curves; (d) Element composition.

exhibited a rapid N_2 uptake at low relative pressure (P/P_0) region of less than 0.05, indicating the microporous structure of activated carbon. However, the N_2 adsorbed capacity of AC-1100–4 and AC-1100–2 still increased to a higher level rather than tended to saturation, and had a large hysteresis loop, implying that there were partial mesopores or even macropores in the ACs (Hou et al., 2020). The ACs had a wide pore size distribution, which was mainly concentrated in the range>1 nm (Fig. 4c). This was consistent with the characteristics of ACs prepared by physical activation (Pena et al., 2020). When activation temperature was lower than 1000 °C, the specific surface area and pore volume of ACs increased gradually, indicating that the development of pore structure was gradually full (Table 2). The microstructures of ACs were able to show some evidence of increased pore development (see Supplementary materials). The higher temperature (>1000 °C) led to the expansion of some micropores into mesopores or the edge of the pores occurred to collapse, resulting in the decrease in micropore volume (Gao et al., 2021). The structure of AC-1200–4 was destroyed, and the collapse of pore structure was also found, resulting in a significant decrease in the specific surface area of ACs (Table 2). Therefore, excessive temperature was not conducive to the production of ACs by self-activation method. Furthermore, the AC-1000–4 had the minimum average pore size (2.1 nm). According to the results of section ***3.2***, H_2O played a more important activation role at low temperatures (≤900 °C) than CO_2. And previous studies showed that the pore size distribution of ACs activated by H_2O was wider than that activated by CO_2 (Pena et al., 2020). The carbon yield decreased from 27 % to 6 % with the increase of temperatures (Table 2). Therefore, the optimum temperature for pyrolysis self-activation was suggested to 1000 °C based on the qualities and yields of ACs. At this temperature, the specific surface area and pore volume of ACs first increased and then decreased with increase in residence times (Table 2). The N_2 adsorption of ACs followed a similar trend (Fig. 4b), owing to the insufficient pore formation reaction in a short time, whereas pore structure was destroyed when the residence time was too long.

Table 2
Porous properties and yield of ACs.

Samples	S_{BET} (m^2/g)	Pore volume (cm^3/g) Total	Micro	*Meso*	Average pore size (nm)	Yield (%)
AC-800–4	373	0.206	0.129	0.054	2.2	27
AC-900–4	869	0.447	0.303	0.142	2.2	21
AC-1000–4	1377	0.726	0.502	0.201	2.1	16
AC-1100–4	1855	1.220	0.312	0.651	2.6	10
AC-1200–4	1360	1.204	0.226	0.688	3.5	6
AC-1000–2	1232	0.611	0.438	0.167	2.0	19
AC-1000–6	1326	0.698	0.473	0.212	2.2	14
AC-1000–8	1314	0.672	0.443	0.199	2.3	13

The carbon content of ACs varied from 89 % to 97 % (Fig. 4d), indicating that the high purity of ACs. Raman spectra of ACs showed both D and G peaks around 1350 cm^{-1} and 1560 cm^{-1} (see Supplementary materials). The intensity ratio of D/G peaks (I_D/I_G) for ACs were 0.95, 0.97, 1.15, 1.11, and 1.08 corresponding to the temperatures of 800 °C, 900 °C, 1000 °C, 1100 °C and 1200 °C. High ratio of I_D/I_G reflected the low graphitization degree of carbon, indicating the highly defective or porous nature of ACs prepared at high activation temperatures (Jiang et al., 2020). Based on the XPS spectrum of AC-1000–4 (see

Supplementary materials), the oxygen element existed in the form of O═C-O (533.9 eV), C-OH (532.8 eV) and C═O (532.1 eV), and the corresponding contents were 19 %, 69 % and 12 %, respectively. High hydroxyl content increased the wettability of carbon materials and their affinity to metal ions to improve the adsorption property (Tran et al., 2017). The peaks located at 284.4 eV, 284.6 eV, 285.8 eV and 287.6 eV represented graphitic carbon (27 %), C-OH (33 %), C═O (25 %) and –COOH (15 %), respectively. The graphitic carbon accounted for a high proportion of AC-1000–4, whose graphite-like structure could act as a π-acceptor and interact with the target pollutant (Wang et al., 2020). These findings demonstrated that self-activation influenced the properties of ACs, with some effects beneficial to pollutants adsorption.

3.4. *Arsenic adsorption*

At the same initial concentration, the arsenic adsorption capacities of ACs were investigated. The arsenic adsorption capacity of AC significantly depended on its specific surface area and pore volume (Fig. 5a-b). The large specific surface area and pore volume provided more adsorption sites for the removal of arsenic, resulting in the adsorption capacity of AC-1000–4 was much higher than that of AC-800–4 and AC-900–4. Micropores acted as active sites for arsenic ions, and the mesopores and macropores acted as channels for arsenic ions diffusion and reservoirs during adsorption process (Hou et al., 2020). It was found that too many mesopores or macropores of AC-1100–4 and AC-1200–4 caused the decrease of arsenic adsorption capacity. The adsorption capacity of As(III) for ACs was lower than that of As(V) at the same conditions, because the electrical neutrality of the As(III) surface was not conducive to the adsorption caused by electrostatic forces (Addo Ntim and Mitra, 2012). The adsorption results indicated that the sample of AC-1000–4 owned a higher arsenic adsorption potential. Therefore, the adsorption capacity of AC-1000–4 under different conditions was further investigated.

Fig. 5c showed that pH significantly influenced As adsorption behavior of AC-1000–4. The pH_{zpc} of AC-1000–4 was 8.3 (see Supplementary materials). The AC possesses a positive surface charge below pH_{zpc}, and negatively charged surface above this value. This resulted in the electrostatic repulsion and attraction between arsenic ions and AC surface thereby affecting the adsorption of arsenic. The environment with strong acid or alkali was not suitable for the removal of arsenic from water. The As(III) and As(V) adsorption of ACs corresponded to different pH ranges because pH value of solution changed the surface charge of ACs and influenced the ionization degree and speciation of arsenic (Mondal et al., 2017).

The As adsorption process of ACs also depended on environmental temperature. With the increase of temperature, the As(III) adsorption capacity of ACs increased from 3.4 mg/g to 4.2 mg/g. Similarly, the As (V) adsorption capacity also increased from 4.4 mg/g to 4.9 mg/g (Fig. 5d). The higher temperatures sped up the As molecule while slowed the retarding forces on the molecules (Mondal et al., 2017). However, the As adsorption capacity of ACs decreased with the further increase of temperatures. This was due to that high temperature increased the kinetic energy of arsenic ions, resulting in partial desorption.

The adsorption capacity of AC-1000–4 increased with the increase of adsorption times (Fig. 5e), because random collisions among the participant particle caused As particles not fully bond with the adsorption sites of ACs in a short time. It was found that the optimum adsorption time was 240 min. The pseudo-second-order kinetics had higher R^2 values than pseudo-first-order kinetics (see Supplementary materials). The theoretical q_e values of As(V) and As(III) from pseudo-second-order model were 5.1 mg/g and 4.6 mg/g, which were close to practical values (5.1 mg/g of As(V) and 4.5 mg/g of As(III)), indicating a chemical adsorption during the arsenic adsorption process (Xiong et al., 2017).

The As adsorption capacity increased when the initial concentration increased from 1 mg/L to 100 mg/L at pH value of 7.0 (Fig. 5f). Under the condition of low As concentration, the ratio of the number of As ions to the effective adsorption position was low, resulting in a relatively low adsorption rate. The adsorption data were fitted by Langmuir and Freundlich equations for the arsenic adsorption isotherm. The maximum adsorption capacities of As(V) and As(III) were 16.0 mg/g and 10.9 mg/g, respectively (see Supplementary materials). Langmuir equation owned a higher R^2 than Freundlich equation, indicating that the monolayer adsorption played a key role in the arsenic uptake (Yu et al.,

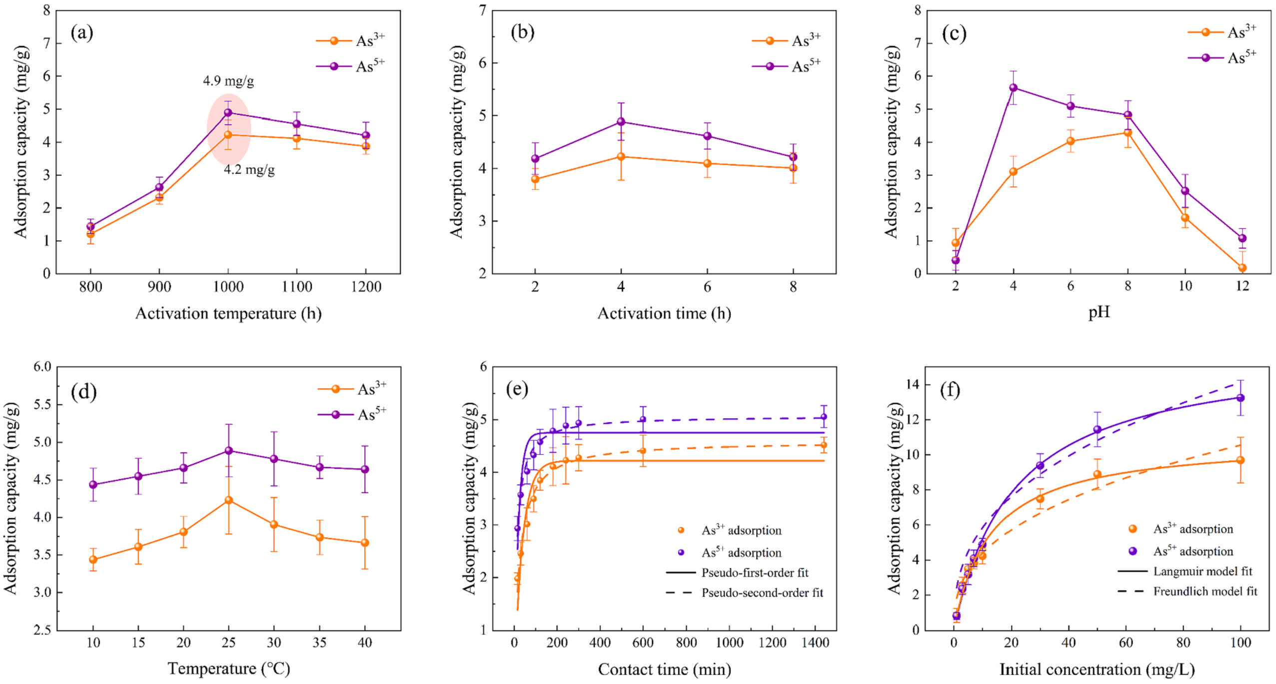

Fig. 5. As adsorption capacity of ACs. (a) Activation temperatures; (b) Activation times; (c) Initial pH of solution; (d) Adsorption temperature; (e) Adsorption kinetics; (f) Adsorption isotherms.

2017).

3.5. Gaseous product

To investigate the effects of self-activation behavior and gas interaction on the final products, the gaseous products were compared with the gas obtained at temperature of 700 °C during pyrolysis self-activation process. The evolution of gaseous products included three steps. The CO, CO_2, CH_4 and H_2 from BSS pyrolysis were released at the first step with temperature of 180–700 °C. The second step (700–1000 °C) involved the consumption of CO_2 and production of H_2 by activation reaction. The interaction of gases throughout the whole self-activation process occurred at the third step. Table 1 summarizes the main reactions (R) of the pyrolysis self-activation process for ease of interpretation. The Gas-A was obtained at temperature of 700 °C, which was regarded as the product of pyrolysis stage due to the insignificant activation reaction and gas recombination. A large amount of CO_2 and a small amount of CO, CH_4 and H_2 were observed in the Gas-A sample, indicating that the gaseous product of BSS pyrolysis was mainly CO_2 (Fig. 6). At the pyrolysis stage, CO_2 and CO were released from decarboxylation and depolymerization or the secondary oxidation of carbon (R2- R5), CH_4 was released by the cracking and depolymerization reactions (R6), and H_2 was also released from the cracking of the volatile matter generated by the pyrolysis and gasification (Yang et al., 2021).

Due to the reaction of H_2O and C, the increase of CO and H_2 content was observed in Gas-B sample. And the activation of CO_2 further increased the content of CO in Gas-C and Gas-D samples, while decreasing the concentration of CO_2. The CH_4 content was mainly determined by the CH_4-reforming reactions (R9-R11) (Yang et al., 2021). The decrease of CH_4 content was due to that the higher temperature was beneficial to shift the equilibrium of CH_4-reforming reactions to hydrogen products. Similarly, it was also used to explain the conversion of H_2 to CO_2 (R12). This confirmed that the activation reaction and H_2-reforming reaction increased CO content. In conclusion, CO (46 %) and H_2 (44 %) were the major gaseous products of Gas-D, which could be used to generate heating for industrial applications. The HHV of gaseous products varied from 10.3 MJ/Nm^3 to 11.7 MJ/Nm^3, which was significantly higher than that of pyrolysis. This was due to the activation reaction increased the concentration of CO and H_2 in the gaseous product. In a word, gaseous products from self-activation process of BSS were a type of clean combustible gases with high HHV, which were further used as fuels during self-activation process. The utilization of these combustible gases could reduce the cost, and effectively improve the economic benefit and commercial attraction of self-activation.

4. Conclusion

The production of ACs by pyrolysis self-activation method not only avoided the use of external chemical or physical activators, but also produced a by-product of combustible gas with a high HHV. The prepared activated carbon owned a better arsenic adsorption potential. Based on pore structure, arsenic adsorption property, and gaseous product, the pyrolysis self-activation process of BSS was activation temperature of 1000 °C for residence time of 4 h. The future work will focus on shortening the residence time of the self-activation process or the further utilization of combustible gas.

CRediT authorship contribution statement

Qi Gao: Data curation, Writing – original draft, Conceptualization, Methodology, Formal analysis, Software. **Zixing Feng:** Data curation, Methodology, Formal analysis, Software. **Yuyu He:** Conceptualization, Methodology. **Yanmei Hou:** Conceptualization, Methodology. **Hao Ren:** Visualization, Investigation, Software. **Mengfu Su:** Visualization, Investigation, Software. **Liangmeng Ni:** Supervision, Validation. **Zhijia Liu:** Conceptualization, Methodology, Resources, Project administration, Funding acquisition, Writing – review & editing.

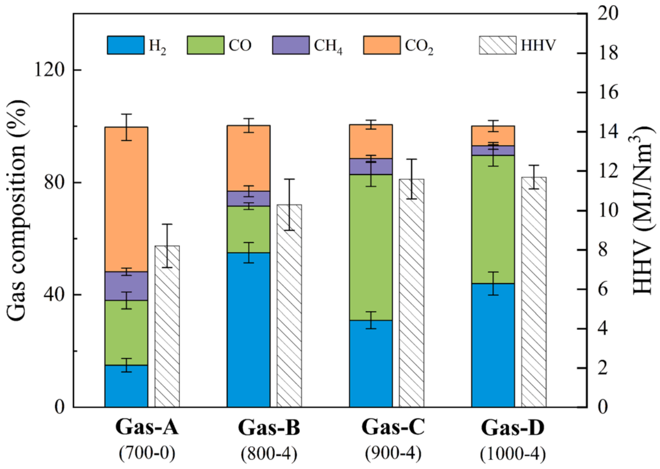

Fig. 6. The composition and HHV of gaseous products from pyrolysis self-activation of BSS.

Declaration of Competing Interest

The authors declare that they have no known competing financial interests or personal relationships that could have appeared to influence the work reported in this paper.

Data availability

No data was used for the research described in the article.

Acknowledgments

This research was financially supported by 'National Natural Science Fundation' (31971742).

Appendix A. Supplementary data

Supplementary data to this article can be found online at https://doi.org/10.1016/j.biortech.2022.128353.

References

Addo Ntim, S., Mitra, S., 2012. Adsorption of arsenic on multiwall carbon nanotube–zirconia nanohybrid for potential drinking water purification. J Colloid Interf Sci. 375, 154–159.

Basile, L., Tugnoli, A., Stramigioli, C., Cozzani, V., 2014. Influence of pressure on the heat of biomass pyrolysis. Fuel 137, 277–284.

Bommier, C., Xu, R., Wang, W., Wang, X., Wen, D., Lu, J., Ji, X., 2015. Self-activation of cellulose: A new preparation methodology for activated carbon electrodes in electrochemical capacitors. Nano Energy 13, 709–717.

Chen, Y.-D., Huang, M.-J., Huang, B., Chen, X.-R., 2012. Mesoporous activated carbon from inherently potassium-rich pokeweed by in situ self-activation and its use for phenol removal. J. Anal. Appl. Pyrol. 98, 159–165.

Chen, R., Lun, L., Cong, K., Li, Q., Zhang, Y., 2019. Insights into pyrolysis and co-pyrolysis of tobacco stalk and scrap tire: Thermochemical behaviors, kinetics, and evolved gas analysis. Energy. 183, 25–34.

Chen, W., Thanapal, S.S., Annamalai, K., Ansley, R.J., Mirik, M., 2013. Updraft gasification of mesquite fuel using air/steam and CO_2/O_2 mixtures. Energy Fuels 27, 7460–7469.

Dong, Z., Liu, Z., Zhang, X., Yang, H., Li, J., Xia, S., Chen, Y., Chen, H., 2019. Pyrolytic characteristics of hemicellulose, cellulose and lignin under CO_2 atmosphere. Fuel 256, 115890.

Gao, Q., Xiang, H., Ni, L., Hou, Y., He, Y., Feng, Z., Yang, J., Hu, W., Liu, Z., 2021. Nitrogen self-doped activated carbons with narrow pore size distribution from bamboo shoot shells. Colloids Surf., A 629, 127408.

Gao, Q., Ni, L., He, Y., Hou, Y., Hu, W., Liu, Z., 2022. Effect of hydrothermal pretreatment on deashing and pyrolysis characteristics of bamboo shoot shells. Energy. 247, 123510.

Gayathiri, M., Pulingam, T., Lee, K.T., Sudesh, K., 2022. Activated carbon from biomass waste precursors: Factors affecting production and adsorption mechanism. Chemosphere 133764.

Hou, Y., Yan, S., Huang, G., Yang, Q., Huang, S., Cai, J., 2020. Fabrication of N-doped carbons from waste bamboo shoot shell with high removal efficiency of organic dyes from water. Bioresour. Technol. 303, 122939.

Jiang, C., Yakaboylu, G.A., Yumak, T., Zondlo, J.W., Sabolsky, E.M., Wang, J., 2020. Activated carbons prepared by indirect and direct CO_2 activation of lignocellulosic biomass for supercapacitor electrodes. Renewable Energy 155, 38–52.

Kleszyk, P., Ratajczak, P., Skowron, P., Jagiello, J., Abbas, Q., Frąckowiak, E., Béguin, F., 2015. Carbons with narrow pore size distribution prepared by simultaneous carbonization and self-activation of tobacco stems and their application to supercapacitors. Carbon 81, 148–157.

Li, X., Mei, Q., Dai, X., Ding, G., 2017. Effect of anaerobic digestion on sequential pyrolysis kinetics of organic solid wastes using thermogravimetric analysis and distributed activation energy model. Bioresour. Technol. 227, 297–307.

Li, L., Wu, M., Song, C., Liu, L., Gong, W., Ding, Y., Yao, J., 2021. Efficient removal of cationic dyes via activated carbon with ultrahigh specific surface derived from vinasse wastes. Bioresour. Technol. 322, 124540.

Mondal, S., Aikat, K., Halder, G., 2017. Biosorptive uptake of arsenic(V) by steam activated carbon from mung bean husk: equilibrium, kinetics, thermodynamics and modeling. Appl Water Sci. 7, 4479–4495.

Omorogie, M.O., Babalola, J.O., Ismaeel, M.O., McGettrick, J.D., Watson, T.M., Dawson, D.M., Carta, M., Kuehnel, M.F., 2021. Activated carbon from Nauclea diderrichii agricultural waste-a promising adsorbent for ibuprofen, methylene blue and CO_2. Adv. Powder Technol. 32, 866–874.

Özsin, G., Pütün, A.E., 2017. Insights into pyrolysis and co-pyrolysis of biomass and polystyrene: Thermochemical behaviors, kinetics and evolved gas analysis. Energy Convers. Manage. 149, 675–685.

Pena, J., Villot, A., Gerente, C., 2020. Pyrolysis chars and physically activated carbons prepared from buckwheat husks for catalytic purification of syngas. Biomass Bioenergy 132, 105435.

Pincus, L.N., Petrović, P.V., Gonzalez, I.S., Stavitski, E., Fishman, Z.S., Rudel, H.E., Anastas, P.T., Zimmerman, J.B., 2021. Selective adsorption of arsenic over phosphate by transition metal cross-linked chitosan. Chem. Eng. J. 412, 128582.

Slimani, R., El Ouahabi, I., Abidi, F., El Haddad, M., Regti, A., Laamari, M.R., Antri, S.E., Lazar, S., 2014. Calcined eggshells as a new biosorbent to remove basic dye from aqueous solutions: Thermodynamics, kinetics, isotherms and error analysis. J. Taiwan Inst. Chem. Eng. 45, 1578–1587.

Sulaiman, N.-S., Hashim, R., Amini, M.-H.-M., Danish, M., Sulaiman, O., 2018. Optimization of activated carbon preparation from cassava stem using response surface methodology on surface area and yield. J. Cleaner Prod. 198, 1422–1430.

Tran, H.N., You, S.-J., Chao, H.-P., 2017. Fast and efficient adsorption of methylene green 5 on activated carbon prepared from new chemical activation method. J. Environ. Manage. 188, 322–336.

Vinayagam, M., Suresh Babu, R., Sivasamy, A., Ferreira de Barros, A.L., 2020. Biomass-derived porous activated carbon from Syzygium cumini fruit shells and Chrysopogon zizanioides roots for high-energy density symmetric supercapacitors. Biomass Bioenergy 143, 105838.

Wang, R.-Z., Huang, D.-L., Liu, Y.-G., Zhang, C., Lai, C., Wang, X., Zeng, G.-M., Zhang, Q., Gong, X.-M., Xu, P., 2020. Synergistic removal of copper and tetracycline from aqueous solution by steam-activated bamboo-derived biochar. J. Hazard. Mater. 384, 121470.

Wu, X., Ba, Y., Wang, X., Niu, M., Fang, K., 2018. Evolved gas analysis and slow pyrolysis mechanism of bamboo by thermogravimetric analysis, Fourier transform infrared spectroscopy and gas chromatography-mass spectrometry. Bioresour. Technol. 266, 407–412.

Xia, C., Shi, S.Q., 2016. Self-activation for activated carbon from biomass: theory and parameters. Green Chem. 18, 2063–2071.

Xia, C., Kang, C., Patel, M.D., Cai, L., Gwalani, B., Banerjee, R., Shi, S.Q., Choi, W., 2016. Pine wood extracted activated carbon through self-activation process for high-performance lithium-ion battery. Chemistry Select. 1, 4000–4007.

Xiong, Y., Tong, Q., Shan, W., Xing, Z., Wang, Y., Wen, S., Lou, Z., 2017. Arsenic transformation and adsorption by iron hydroxide/manganese dioxide doped straw activated carbon. Appl. Surf. Sci. 416, 618–627.

Yang, P., Zhao, S., Zhang, Q., Hu, J., Liu, R., Huang, Z., Gao, Y., 2021. Synergistic effect of the cotton stalk and high-ash coal on gas production during co-pyrolysis/gasification. Bioresour. Technol. 336, 125336.

Ye, L., Zhang, J., Zhao, J., Tu, S., 2014. Liquefaction of bamboo shoot shell for the production of polyols. Bioresour. Technol. 153, 147–153.

Yin, Y., Zhou, T., Luo, H., Geng, J., Yu, W., Jiang, Z., 2019. Adsorption of arsenic by activated charcoal coated zirconium-manganese nanocomposite: Performance and mechanism. Colloids and Surfaces A: Physicochemical and Engineering Aspects. 575, 318–328.

Yu, Y., Zhang, C., Yang, L., Paul Chen, J., 2017. Cerium oxide modified activated carbon as an efficient and effective adsorbent for rapid uptake of arsenate and arsenite: Material development and study of performance and mechanisms. Chem. Eng. J. 315, 630–638.

Zhong, D., Ren, S., Dong, X., Yang, X., Wang, L., Chen, J., Zhao, Z., Zhang, Y., Tsang, D.C. W., Crittenden, J.C., 2021. Rice husk-derived biochar can aggravate arsenic mobility in ferrous-rich groundwater during oxygenation. Water Res. 200, 117264.

Zoroufchi Benis, K., Soltan, J., McPhedran, K.N., 2021. Electrochemically modified adsorbents for treatment of aqueous arsenic: Pore diffusion in modified biomass vs. biochar. Chem. Eng. J. 423, 130061.